Transport in Porous Media (2019) 126:579–598
https://doi.org/10.1007/s11242-018-1130-2

Fractal and Multifractal Characteristics of Pore Throats in the Bakken Shale

Kouqi Liu[1] · **Mehdi Ostadhassan**[1] · **Lingyun Kong**[1]

Received: 5 May 2018 / Accepted: 27 July 2018 / Published online: 3 August 2018

Abstract
To evaluate pore structures of the Bakken Shale, which is one of the most important factors that affect petrophysical properties, high-pressure mercury intrusion was employed in this study. Pore structures such as pore-throat size, pore-throat ratio, and fractal attributes are investigated in this major shale play. Pore-throat size from 3.6 to 200 um is widely distributed in these shale samples. Accordingly, pore-throat size distributions demonstrate the multimodal behavior within the samples. The whole pore-throat network can be divided into four clusters: one set of large pores, two transitional/intermediate pore groups, and one set of smaller pores. The fractal analysis revealed that fractal dimensions decrease as the pore-throat size decreases. The multifractal analysis demonstrated that as the maturity of the shale samples increases, pore-throat size distributions would become more uniform and pore structures tend to become more homogeneous. The results are compared to our previous results obtained from nitrogen gas adsorption for further verifications of fractal behavior. Finally, although fractal analysis of mercury intrusion and nitrogen gas adsorption were comparable, the results of multifractal analysis from these two methods were not identical.

Keywords Shale · Pore-throat size · Mercury intrusion · Fractal · Multifractal

1 Introduction

Unconventional shale formations (including shale oil and shale gas) have become a major source of hydrocarbon production in recent years (Hu et al. 2017). Shale is a fine-grained, clastic sedimentary rock which is usually composed of a mixture of clay and other minerals such as quartz, feldspar, and calcite (Blatt et al. 2006). Compared with conventional plays, shale reservoirs have lower porosity and permeability which makes them to categorized under unconventional reservoir (Liu et al. 2017a; Zhang et al. 2017; Li et al. 2017a). Storage and flow of hydrocarbons through such formations is controlled by the capillary entry pressure,

✉ Kouqi Liu
kouqi.liu@ndus.edu

✉ Mehdi Ostadhassan
mehdi.ostadhassan@engr.und.edu

[1] Department of Petroleum Engineering, University of North Dakota, Grand Forks, ND 58202, USA

the permeability and the extent of the diffusive losses through the pore spaces (Schlömer and Krooss 1997; Schmitt et al. 2013; Yang et al. 2016). Therefore, a better understanding of pore structures/network of these shale formations can assist in evaluating the overall reservoir production performance.

High-pressure mercury intrusion is an extremely useful characterization technique for porous materials and is considered as one of the few methods that can acquire data over a broad dynamic range of pore sizes using a single theoretical model (Webb 2001; Giesche 2006). With the strong characterization capabilities, high-pressure mercury intrusion can measure capillary diameter in ranges from 3.6 nm to 360 um which is considered a wide interval of pore sizes in porous rocks. This is far beyond what nitrogen gas adsorption can detect which is limited to pore sizes less than 200 nm. High-pressure mercury intrusion has been widely applied in characterizing pore structures of coal (Peng et al. 2017; Zhou et al. 2017; Yu et al. 2018), carbonate (Ding et al. 2017), shale oil reservoir (Hu et al. 2017), shale gas reservoir (Schmitt et al. 2013; Labani et al. 2013) and tight oil sandstone (Li et al. 2017b).

Other researchers and we have shown that micropore structures of shale formations are very complex with a wide range of pore sizes from nano to macro-meters in diameter (Chen and Xiao 2014; Liu et al. 2017a, b, 2018a). These complex pore structures sometimes can't be modeled by traditional Euclidean geometry (Lopes and Betrouni 2009). In this case, fractal theory which is introduced by Mandelbrot (1983) has now become a powerful tool to characterize pore size distributions (Liu et al. 2017a; Liu and Ostadhassan 2017; Xia et al. 2018) and electrical conductivity (Cai et al. 2017) of shale formations. According to the theory of fractal geometry, the fractal dimension of the surface varies between 2 and 3. If the fractal dimension value is close to 3, it indicates that the pore structures are very complex (Thompson et al. 1987). However, the single fractal dimension can only represent the complexity of pore structures and suffers from quantifying heterogeneities of overall pore network of shale rocks. The latest one can be studied via multifractal analysis (Liu et al. 2018b). Multifractal analysis is the extension of fractal analysis which uses a set of generalized dimensions instead of the single dimension, D, common in fractal analysis. Multifractal analysis has been applied in the study of pore structures of mercury intrusion data from soil (Paz Ferreiro et al. 2010) and coal samples (Yu et al. 2018) and has shown great potential in providing us with in-depth information regarding pore structures compared to single fractal theory.

In previous attempts, we applied both fractal and multifractal methods to analyze pore structures of the Bakken Shale samples on the data that was collected by gas adsorption (Liu et al. 2018b). In this study, high-pressure mercury intrusion capillary pressure data is used to characterize pore structures of the Bakken shale. The purpose of this study is to address the following questions: (1) What are the pore-throat characteristics of the Bakken shale? (2) What is the fractal dimension and heterogeneity of the Bakken shale pore network using high-pressure mercury intrusion method? (3) Is there any correlation and meaningful relationship between fractal information from high-pressure mercury intrusion and low temperature nitrogen adsorption?

2 Experiments and Modeling

The schematic of the whole process will include the following steps: first, we chose the samples and derived the basic properties of the samples (mineral compositions and geochemistry properties); Then, we calculated the pore-throat distributions and analyzed the characteristics

of the pore throats of the samples from high-pressure mercury injection; After that, we quantified the fractal behavior and the multifractal behavior of the pore-throat distributions. Finally, we compared the fractal behaviors and multifractal behaviors and found their correlations.

2.1 Samples and Experiments

Five samples from the Bakken Formation were collected and then analyzed with X-ray diffraction (XRD) for mineralogical compositions along with Rock–Eval pyrolysis to quantify total organic carbon (TOC) content and thermal maturity (Liu et al. 2018a). For the high-pressure mercury intrusion, all the samples were first vacuum-dried at 70 °C in the oven for more than 10 h and then were moved to the mercury porosimeter (Auto Pore IV 9510, Micrometrics Instrument). The injection pressure was increased from 0 up to 60,000 psi (413.68 MPa) to obtain the relevant capillary pressure versus mercury saturation data.

2.2 Single Fractal Analysis

2.2.1 Geometric Fractal Dimension

The number of pore throat with the radius greater than r is counted as N ($>r$) if the attribution of pore-throat radius conformed with fractal structure. Then, N can be expressed as (Mandelbrot et al. 1984):

$$N(>r) = \int_{r}^{r_{\max}} P(r)\mathrm{d}r = ar^{-D} \tag{1}$$

where $r_{\max}$ is the maximum pore-throat radius, $P(r)$ is the distribution density function of the pore-throat radius, a is a constant, and D is the fractal dimension. If the pores are assumed as bundles of capillary tubes with radius r and the radius is equal to the length of the tube l, then the pore volume can be calculated as (Zhang and Weller 2014):

$$V = N\pi r^3 = a\pi r^{3-D} \tag{2}$$

Then

$$\frac{\mathrm{d}V}{\mathrm{d}r} = a(3-D)\pi r^{2-D} \tag{3}$$

Then, the total pore volume of the porous rock with pore sizes less than r will be:

$$V(<r) = \int_{r_{\min}}^{r} a(3-D)\pi r^{2-D}\mathrm{d}r = a\pi\left(r^{3-D} - r_{\min}^{3-D}\right) \tag{4}$$

In this regard, the total pore volume will be expressed as:

$$V = \int_{r_{\min}}^{r_{\max}} a(3-D)\pi r^{2-D}\mathrm{d}r = a\pi\left(r_{\max}^{3-D} - r_{\min}^{3-D}\right) \tag{5}$$

Then, we will have:

$$1 - S_g = \frac{V(<r)}{V} = \frac{r^{3-D} - r_{\min}^{3-D}}{r_{\max}^{3-D} - r_{\min}^{3-D}} \tag{6}$$

where S_g is the mercury saturation, if $r_{\min} \ll r$, and the following equation can be obtained:

$$1 - S_g = \frac{r^{3-D}}{r_{\max}^{3-D}} \tag{7}$$

As we know, the capillary pressure is inversely proportional to the radius of the pores based on the modified Young–Laplace equation. As P_c decreases, r will reach a maximum value and increases; therefore, the equation can be transformed into:

$$1 - S_g = \frac{P_c^{3-D}}{P_{c\min}^{3-D}} \tag{8}$$

By taking the logarithm of both sides of the above equation, the following relationship will be achieved:

$$\log(1 - S_g) = (3 - D)\log P_C - (3 - D)\log P_{c\min} \tag{9}$$

This will create a linear relationship between, $\log(1 - S_g)$ and $\log P_c$. Hence, the fractal dimension can be directly calculated from the slope of this cross-plot.

2.2.2 Thermal Dynamic Fractal Dimension

The model that was referred to in Sect. 2.2.1 is called the geometry model. However, sometimes the fractal dimension from these models is larger than 3 which is beyond fractal dimension value based on the theory of fractal geometry (ranges from 2 to 3). Alternatively, another single fractal model—the thermal dynamic model—proposed by Zhang and Li (1995) which is based on the energy characteristics should be used in such scenarios, which is the case here, and the results are compared to fractal dimensions calculated from the geometry model:

$$\ln(W_n) = C + \ln(Q_n) \tag{10}$$

where n is the nth stage of the pressure in the process of mercury intruding the pores. Q_n and W_n can be derived using the following two equations:

$$Q_n = r_n^{2-D_w} V_n^{D_w/3} \tag{11}$$

$$W_n = \sum_{i=1}^{n} \overline{P_i} \Delta V_i \tag{12}$$

where r_n is the radius of the nth stage of the pressure, and V_n is the total intrusion volume at the nth stage of pressure. P_i is the average pressure between two neighboring stages of pressure ($P_{i-1} - P_i$), ΔV_i is the intruded volume ($V_i - V_{i-1}$), and D_w is the surface fractal dimension. This will generate a series of Q_n and W_n when n equals to 1, 2, 3, etc. If we plot the $\ln(W_n)$ versus $\ln(Q_n)$ and get the slope of the curve, (f) then this slope would vary as a function of D_w. Using an iteration method, we adjusted D_w until the slope (f) is equal to 1, later, D_w value will be representing the surface fractal dimension.

2.3 Multifractal Analysis

The detailed multifractal analysis procedure can be found in our previous studies which are focused on the gas adsorption data analysis (Liu et al. 2018b). Briefly, a set of boxes with equal length (ε) are applied to the pore size distribution data.

The pore radius of samples can be calculated by Washburn equation (Washburn 1921):

$$P_c = -\frac{2\sigma \cos\theta}{r} \tag{13}$$

where σ is the surface tension of mercury, and θ is the contact angle between mercury and the solid (140° was used in this study). In this study, the intervals of the pore size will be [3.6 nm, 200 um]. The density function fits a power law relationship as explained by Russel et al. (1980) and Chaudhuri and Sarkar (1995):

$$P_i(\varepsilon) \sim \varepsilon^{\alpha_i} \tag{14}$$

where i is the index for each box laid over the set for a ε, $P_i(\varepsilon)$ is the probability of mass at i relative to the total mass for a box size. $N_i(\varepsilon)$ is the number of mass in any box, i at the box size ε, and N_ε is the total number of boxes that contained the mass greater than 0 for each ε. Then, the total mass in all boxes for this ε can be calculated as:

$$N_T = \sum_{i=1}^{N_\varepsilon} N_i(\varepsilon) \tag{15}$$

Then

$$P_i(\varepsilon) = \frac{N_i(\varepsilon)}{N_T} \tag{16}$$

q is defined as an arbitrary range of values (from − 10 to 10) to use as exponents for distorting the data set. For the box size ε, the sum of all mass probabilities distorted by being raised to this q can be calculated as (Posadas et al. 2001):

$$I_{q(\varepsilon)} = \sum_{i=1}^{N_\varepsilon} P_i(\varepsilon)^q \tag{17}$$

For the box size ε, the magnitude of distorted mass probability at a specific box compared to the distorted sum of all boxes can be quantified as:

$$u_i(q, \varepsilon) = \frac{P_i(\varepsilon)^q}{I_{q(\varepsilon)}} \tag{18}$$

Like $P_i(\varepsilon)$, $I_{q(\varepsilon)}$ also fits the power law function which can be written as (Ferreiro et al. 2009):

$$I_{q(\varepsilon)} \sim \varepsilon^{\tau(q)} \tag{19}$$

Then, τ_q can be calculated as:

$$\tau_q = \lim_{\varepsilon \to 0}\left(\frac{\log I_{q(\varepsilon)}}{\log \varepsilon}\right) \tag{20}$$

D_q can be calculated as:

$$D_q = \frac{\tau_q}{q-1} = \frac{\lim_{\varepsilon \to 0}\left(\frac{\log I_{q(\varepsilon)}}{\log \varepsilon}\right)}{q-1} \tag{21}$$

If $q = 1$,

$$D_1 = \lim_{\varepsilon \to 0}\left(\sum_{i=1}^{N(\varepsilon)} p_i(\varepsilon) \ln p_i(\varepsilon)\right) / \ln(\varepsilon) \tag{22}$$

Table 1 Mineral compositions and maturity of the samples

Samples	Quartz (wt%)	Pyrite (wt%)	Feldspar (wt%)	Dolomite (wt%)	Clays (wt%)	VRo-Eq (%)
Sample 1	70.30	3.15	7.70	0.00	18.81	0.56
Sample 2	54.30	8.07	0.00	8.80	28.60	0.56
Sample 3	66.90	2.44	14.40	0.00	16.20	0.63
Sample 4	70.00	2.35	5.50	0.00	22.20	0.63
Sample 5	36.10	8.50	3.40	0.00	52.00	0.92

3 Results and Discussions

3.1 Sample Compositions Analysis

The basic information of the samples that were analyzed in this study is shown in Table 1 [Sample 1–4 are the same samples we analyzed in our previous study (Liu et al. 2018c)]. Quartz (36.1 to 70.3 wt%) and clay minerals (16.2 to 52 wt%) are the two major mineral components of the shale samples. Sample 5 with the smallest amount of quartz has the most clay minerals content. The maturity index shows that Sample 5 is the most mature among all the samples.

3.2 MICP Curve Analysis

The mercury intrusion curves of five samples in this study are shown in Fig. 1. As we can see, when the intrusion pressure increases, the mercury will be forced into the large pores and then small pores. The related mercury saturation value will increase. For Sample 1, 2, 3 and 4, the intrusion curves can be divided into three different stages. As the mercury was injected into the samples, the injection pressure will increase fast as the saturation increases and then followed by a steady slow increase as the saturation becomes larger than a critical point (around 20%). For Sample 5, the pressure increases steadily as the saturation increases from 0 for the whole intrusion process. The difference in the overall form of these curves of five samples indicates that there exists a major difference between their pore structures. For example, as the mercury intrusion pressure reaches 100 kPa, the mercury saturation of all five samples will be 6.59, 8.91, 9.4, 9.26 and 18.19%, respectively. This indicates the percentage of larger pores (>15 μm) in Sample 5 is the most significant and around 3 times the value of the largest pores in Sample 1. However, the percentage of larger pores (>15 μm) in Samples 2, 3 and 4 are found to be very close.

For the extrusion part, the saturation value of all the samples will decrease as the extrusion pressure decreases. Hysteresis between the intrusion and the extrusion is observed for all samples. If all pores are ideally uniform and cylindrical in shape and the intrusion and extrusion of the contact angles are known, then hysteresis could not be expected since the intrusion and the extrusion process are controlled by the same mechanism and exact known parameters (Webb 2001). However, in reality, most samples do not have the ideal pore geometry. As the mercury retracts from the pore system, the new mercury interfaces will be created, and additional energy is needed to get mercury out of the pores. During the intrusion process, a pore is filled with mercury not only due to the pore size being equal or larger than the corresponding pressure but also because of a continuous path that mercury needs to follow

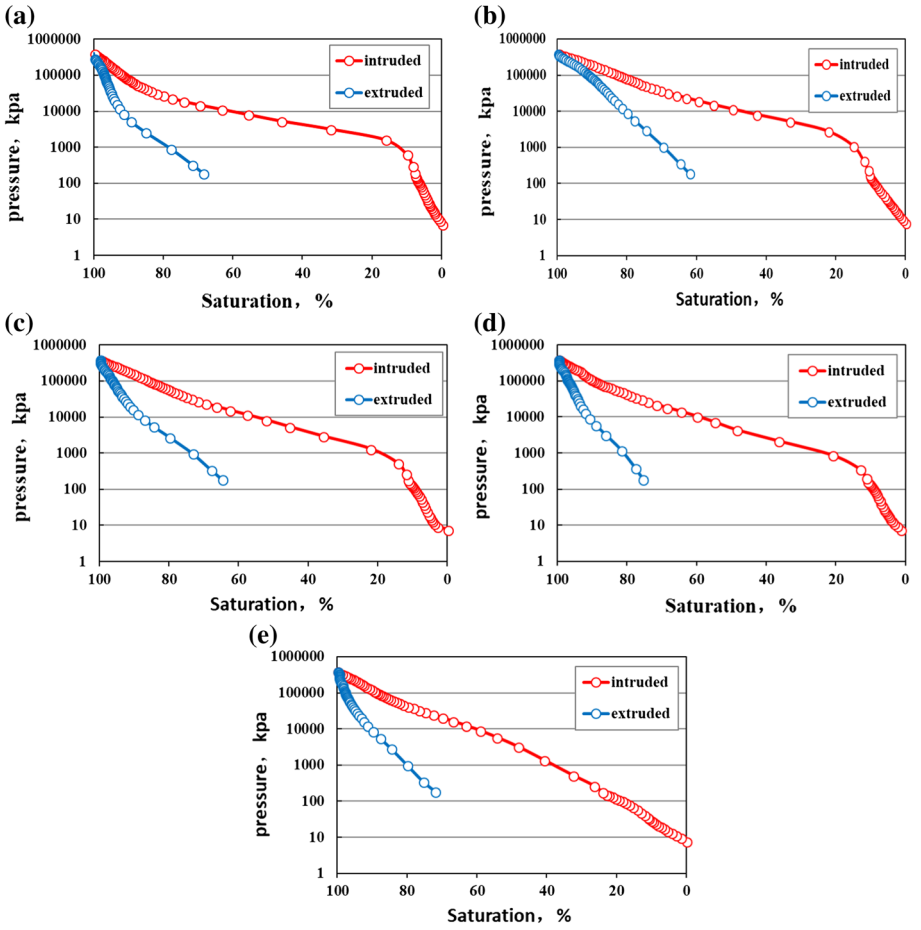

Fig. 1 The mercury intrusion curves of the five samples. a Sample 1, **b** Sample 2, **c** Sample 3, **d** Sample 4 and **e** Sample 5

to get to that specific pore. The large internal pores which are surrounded by smaller ones can only get filled until the pressure is sufficient to fill and follow a pathway toward that pore completely. During the extrusion process, the reverse phenomenon occurs. Those filled internal pores or isolated pores will remain filled with the trapped mercury if they do not own a continuous path toward the sample surface for mercury to leave them (Giesche 2006). The mercury withdrawal efficiency of these samples was calculated from 24.25 (Sample 4) to 37.61% (Sample 2), indicating the complex pore network of these shales.

3.3 Pore-Throat Size Distribution from Mercury Intrusion Analysis

Figure 2 shows pore-throat size distribution of all samples calculated from the above equation. Based on the analysis, the pore-throat size of samples is found to vary from a few nanometers to a few hundred micrometers which is considerably beyond the ability of nitrogen gas adsorption to detect (less than 200 nm). The pore-throat size distribution (PSD) curves of

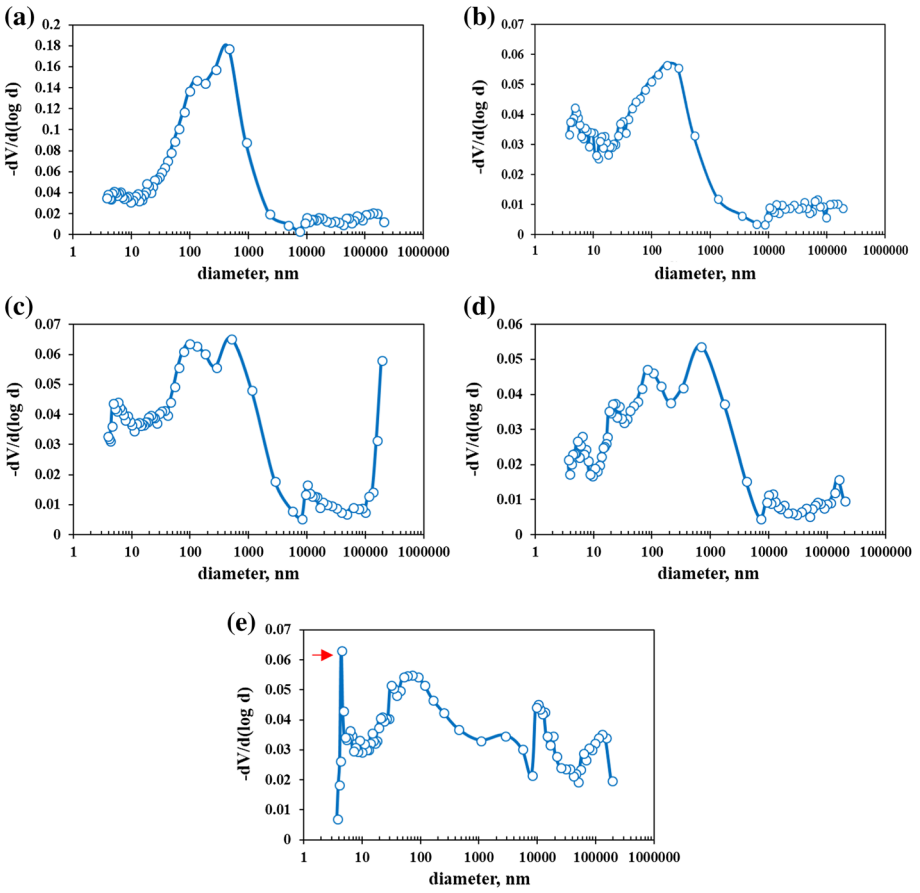

Fig. 2 Pore-throat size distributions of the samples from mercury analysis. **a** Sample 1, **b** Sample 2, **c** Sample 3, **d** Sample 4 and **e** Sample 5

all samples confirm the multimodal behavior which indicates the presence of more than one pore cluster in the pore structures of these shale samples. In this regard, Sample 5 compared to others has a larger peak intensity around pore size of 4.35 nm, indicating the dominance of nanopores with a size around 4.35 nm in this specific sample. Nanopores with sizes around 3 nm are widely distributed in the clay minerals (Kuila et al. 2014). Therefore, if the sample has larger clay content (for example Sample 5 in this study), we would expect more nanopores to be detected. As a result, we will have a more intense peak shown with red arrow in Fig. 2.

The intrusion of the mercury into the pores is controlled by the pore throat, while the radius of the pore and its connectivity controls the extrusion of mercury from the pore. The pore-throat ratio can be used to characterize the relationship between pore throat and pores radius. Figure 3 displays the relations between mercury saturation and the pore-throat ratio. Pore throats with size less than 1000 nm (1 um) are widely distributed in these samples. Sample 1 and Sample 2 had the lowest maturity and the pore throats with size less than 1000 nm (1 um) occupying around 85% of the total pore volume. As the maturity increases, the pore throat with size less than 1000 nm (1 um) seems to occupy around 75% of the total

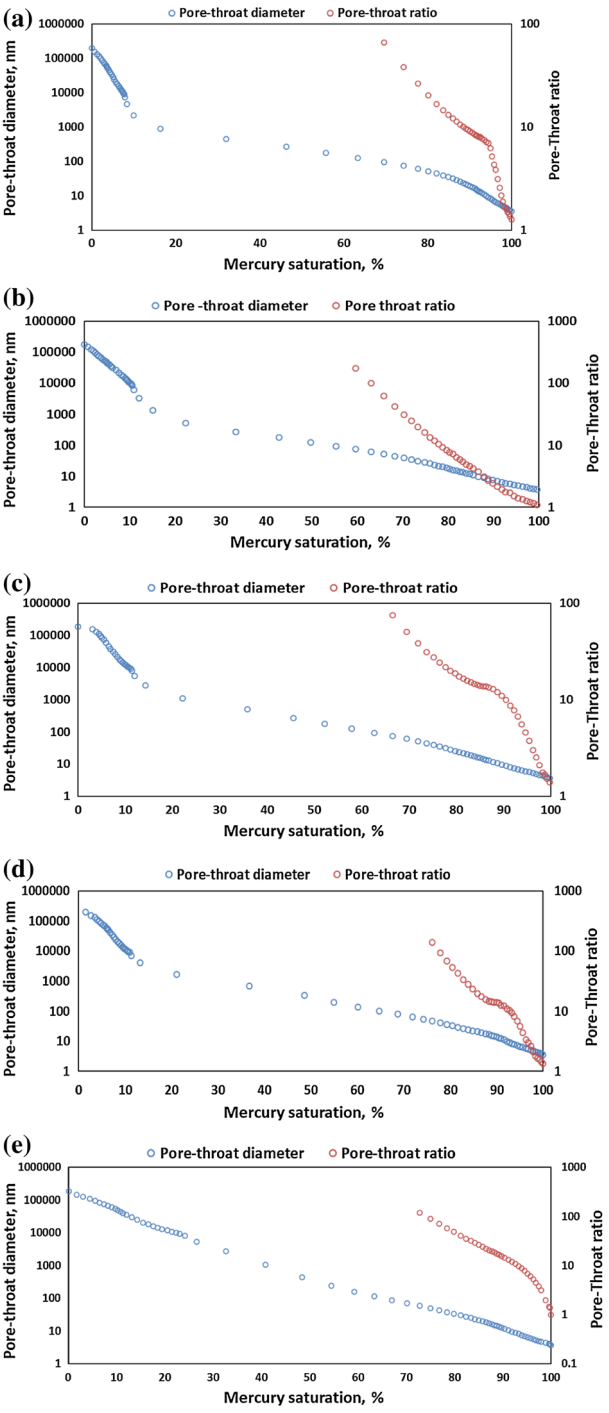

Fig. 3 Correlations between the mercury saturation and pore-throat ratio of the shale samples. **a** Sample 1, **b** Sample 2, **c** Sample 3, **d** Sample 4 and **e** Sample 5

pore volume (Sample 3 and Sample 4). Considering Sample 5 with the highest maturity level, only 60% of total pore volumes is representing pores throat with size less than 1000 nm.

Overall, as the maturity increases, the percentage of the ratio of larger pores over total pore volume of these shale samples will increase. A closer look at Fig. 3 confirms even samples at almost the same maturity level and would exhibit dissimilar pore structures. Considering Sample 1 and Sample 2 for example, only 6% of the total pore volume is made of pore throat with size less than 10 nm in Sample 1 and less than 10 nm comprised almost 13.38% of the total pore volume of Sample 2. The largest pore-throat ratio of Sample 1 was found 66.1, while for Sample 2 the largest pore-throat ratio is 174.7. All these differences indicate that thermal maturity is not only the sole governing factor on pore structure characteristics but also some other controlling components such as mineral compositions could play an important role on various attributes of pore structures. Pore-throat ratio decreases as the pore-throat size decreases which is consistent with the results found by other researchers (Hu et al. 2017).

The threshold pressure P_t can be obtained as the inflection point from the plot of log differential intrusion versus intrusion pressure on logarithmic scale (Hu et al. 2017). The inflection point can be used to explain a connected pore network. Figure 4 illustrates that each sample has several inflection points, demonstrating that different pore networks exist in those samples. Sample 3 for example, the first inflection point reflects the micro fractures or laminae in the samples with the threshold pressure of 0.013647 MPa with corresponding pore-throat diameter L_t of 107 um, while the fifth inflection point reflects nanopore structures in the samples mainly hosted within minerals with the threshold pressure of 335.63 MPa, corresponding to pore-throat diameter L_t of 4.38 nm. Among all the five curves in Fig. 4 that are obtained from different samples, the log differential intrusion versus intrusion pressure curve of Sample 5 is more uniformly distributed.

3.4 Fractal Analysis

In order to present the fractal characteristics of pore structures in the shale samples based on the mercury injection analysis, the cross-plot of $\log(1-S_g)-\log(P_c)$ for all samples was constructed. Figure 5 shows the example of such plot for Sample 4. A good fit with a high correlation coefficient shows that pore structures of Sample 4 have fractal behavior. The curves from all samples overall can be divided into four segments shown in different colors: the smallest absolute value for the slope represents the largest pores, while the largest absolute value of the slope can denote the smallest pores. The remaining two segments which have the absolute value in between the smallest and the largest are transitional/intermediate pores. The fractal analysis results of all samples can be found in Table 2. D_l which can reflect the large pores have the value larger than 2.9 while D_s which represents the small pores are closer to 2. $D_l > D_{t1} > D_{t2} > D_s$, indicating that the complexity of small pores in these samples is overall less than transitional and large pores. We further compared the fractal dimensions of D_l and D_s. We were not able to establish any meaningful correlations between D_l and D_s, which means that samples with greater complexity of larger pore structures will not necessarily have very complex small pore structures, and these two are independent of one another (Fig. 6).

Based on the weighted average of the porosity from larger, transitional and small pores, the total fractal dimension of the whole pore throats of our shale samples was calculated by (Li et al. 2017b):

$$D_a = D_l \frac{\varphi_l}{\varphi_l+\varphi_{t1}+\varphi_{t2}+\varphi_s} + D_{t1} \frac{\varphi_{t1}}{\varphi_l+\varphi_{t1}+\varphi_{t2}+\varphi_s} + D_{t2} \frac{\varphi_{t2}}{\varphi_l+\varphi_{t1}+\varphi_{t2}+\varphi_s} + D_s \frac{\varphi_s}{\varphi_l+\varphi_{t1}+\varphi_{t2}+\varphi_s} \quad (23)$$

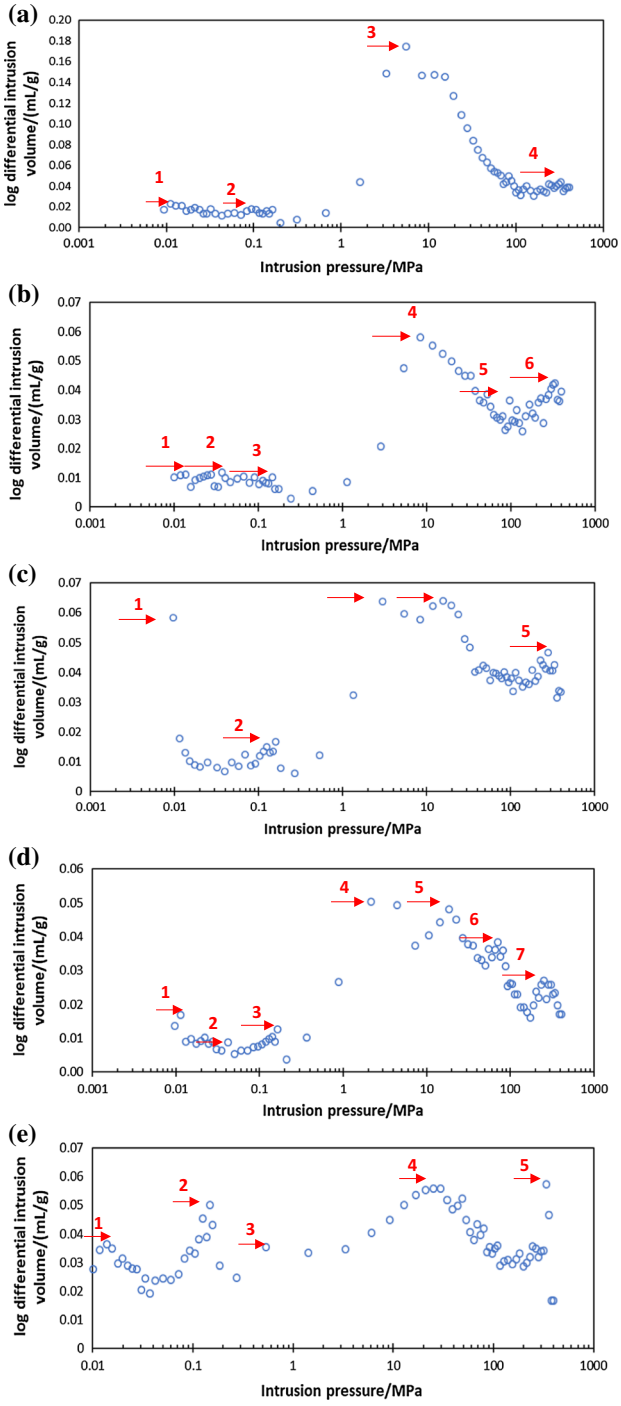

Fig. 4 Log differential intrusion versus intrusion pressure for the testing samples. **a** Sample 1, **b** Sample 2, **c** Sample 3, **d** Sample 4 and **e** Sample 5

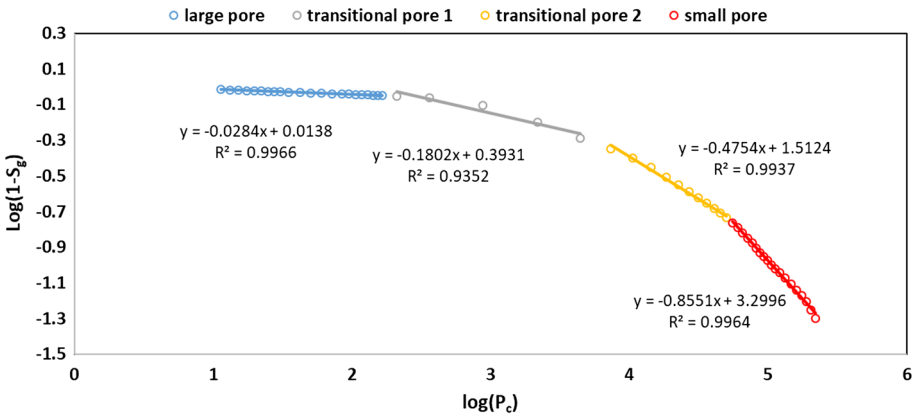

Fig. 5 Fractal dimension curve of Sample 4

Table 2 Fractal analysis of the samples

	Large pore		Transitional pore 1		Transitional pore 2		Small pore	
	D_l	R^2	D_{t1}	R^2	D_{t2}	R^2	Ds	R^2
Sample 1	2.9753	0.9969	2.9547	0.8903	2.3643	0.9949	2.0953	0.9884
Sample 2	2.9633	0.9996	2.9132	0.8492	2.5378	0.9976	2.1627	0.9789
Sample 3	2.9709	0.9942	2.7369	0.9977	2.5171	0.9984	2.0399	0.9813
Sample 4	2.9716	0.9966	2.8198	0.9352	2.5246	0.9937	2.1449	0.9964
Sample 5	2.9160	0.9904	2.8485	0.9920	2.4868	0.9883	2.0933	0.9858

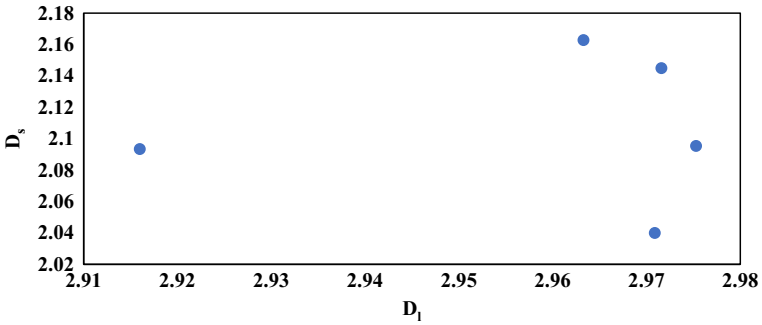

Fig. 6 Correlations between D_l and D_s

where D_l, D_{t1}, D_{t2}, D_s are fractal dimensions which can be found in Table 2. φ_l, φ_{t1}, φ_{t2} and φ_s are the porosity value of large, transitional pore 1, transitional pore 2 and small pores, respectively. The total fractal dimension (D_a) of all samples is presented in Fig. 7. The D_a value of all samples varies between D_{t1} and D_{t2}. Sample 1 has the smallest D_a, while Sample 5 with the largest maturity value has the largest value. The difference between D_a value among the samples are due to the combination of the differences from fractal dimensions D_l, D_{t1}, D_{t2}, D_s and the porosity percentage of each pore cluster. Considering Sample 1 and Sample 5 for example, φ_l and φ_s of Sample 5 are larger than the φ_l and φ_s values of Sample

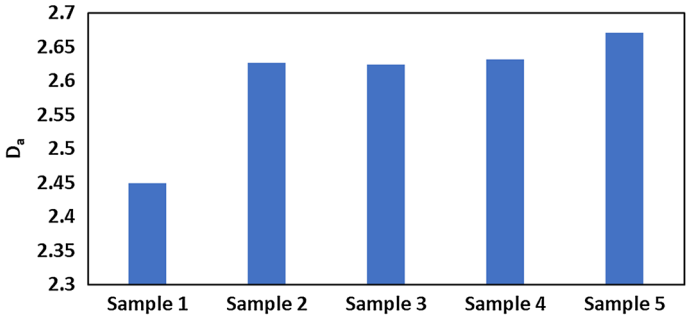

Fig. 7 D_a of all the samples

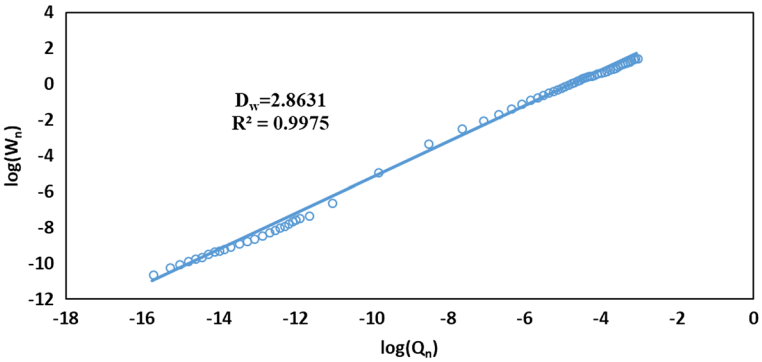

Fig. 8 Linear correlation between Q_n and W_n under D = 2.8631 for Sample 4

1, respectively, indicating Sample 5 has more significant percentage of larger and smaller pores at the same time than Sample 1. Thus, the weighted average of the larger and smaller pores of Sample 5 is overall greater than Sample 1.

Figure 8 shows the analysis results of fractal dimensions of Sample 4 using the thermodynamic model. Linear correlations can be found between Q_n and W_n. D_w of all samples was calculated and compared with the D_a, D_l, D_{t1}, D_{t2} and D_s. There were not any clear correlations between these parameters (Fig. 9). This demonstrates that we need to emphasize which model we apply for fractal analysis. This is since each model can provide us with different results and if the purpose is to compare fractal dimension of the samples, consistency in the model that is being used is necessary to make the results more accurate.

3.5 Multifractal Analysis

The partition functions $u_i(q, \varepsilon)$ can be obtained through boxes with a set of ε and statistical moment q. Figure 10 displays that linear correlations can be found between $u_i(q, \varepsilon)$ and ε which are plotted in a log–log format for Sample 1. For $q < 0$, we can find that $\log u_i(q, \varepsilon)$ increases as $\log(1/\varepsilon)$ increases, whereas $\log u_i(q, \varepsilon)$ decreases as $\log(1/\varepsilon)$ increases when q is larger than 1. A very good linear correlation for all samples with R^2 of about 0.90, demonstrates that our shale samples have perfect PSD multifractal characteristics (Li et al. 2015; Liu et al. 2018b).

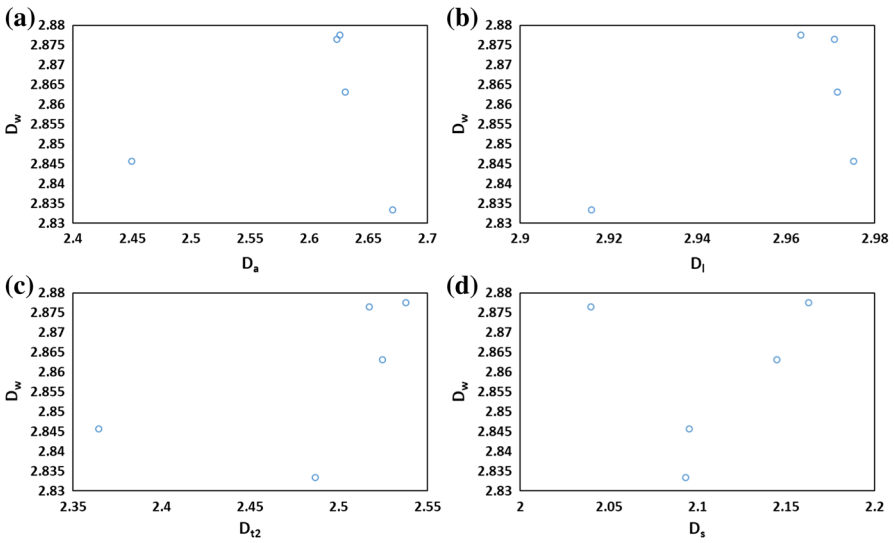

Fig. 9 Comparison of D_w and other fractal dimensions. **a** D_a, **b** D_1, **c** D_{t2} and **d** D_s

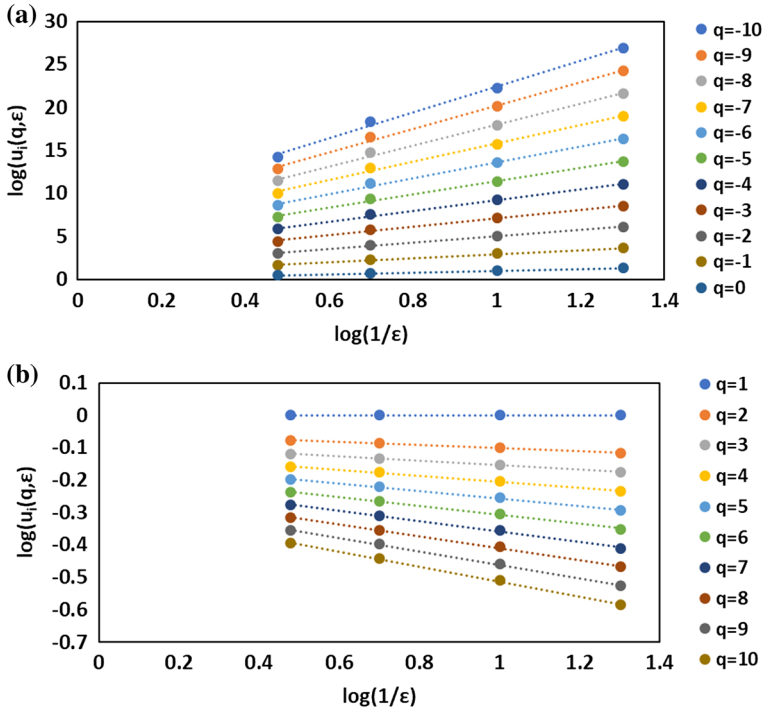

Fig. 10 Log–log plots of the partition function versus box scale of Sample 1. **a** $q \leq 0$ and **b** $q > 0$

The generalized dimensions of all samples are calculated and shown in Fig. 11. D_q follows a monotonic decreasing trend with respect to q which is also an indicator that pore size

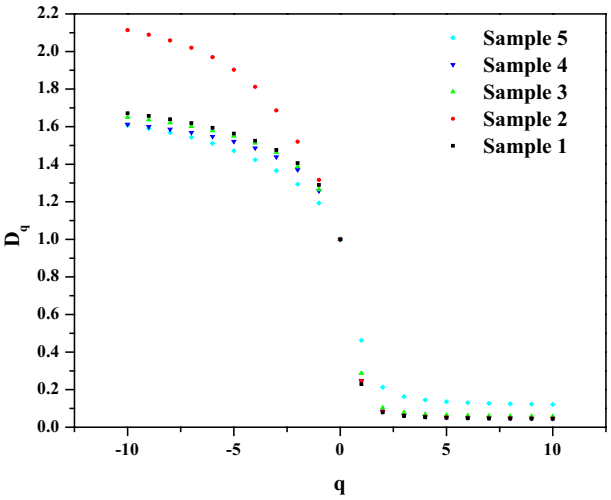

Fig. 11 Correlations between D_q and q

Table 3 The generalized dimension spectrum of all the samples

	D_{-10}	D_0	D_1	H	D_{10}	D_{-10}–D_0	D_0–D_{10}	D_{-10}–D_{10}
Sample 1	1.6712	0.9997	0.2287	0.5208	0.0442	0.6715	0.9555	1.627
Sample 2	2.1137	0.9997	0.2456	0.5218	0.047	1.114	0.9527	2.0667
Sample 3	1.6499	0.9997	0.2871	0.5264	0.0573	0.6502	0.9424	1.5926
Sample 4	1.6122	0.9997	0.2476	0.5217	0.0469	0.6125	0.9528	1.5653
Sample 5	1.6073	0.9997	0.4627	0.5606	0.1208	0.6076	0.8789	1.4865

distributions derived from mercury intrusion have the multifractal behavior. The commonly used D_q parameters such as D_0, D_1, H [which is defined as $(D_2 + 1)/2)$], D_{-10} and D_{10} are also listed in Table 3. D_1, information dimension attributes the concentration degree of the pore size distribution along the whole pore-throat size intervals in our study (Li et al. 2015). The smaller (D_0–D_1) value is, the more uniform the pore size distribution of the sample should be. Sample 5 with the largest maturity index has the smallest D_0–D_1 value (0.537), indicating that pore size distribution of Sample 5 is the most uniform among all. Sample 1 and Sample 2 have the same maturity index with an average D_0–D_1 value of 0.763 which is larger than the average value for Sample 3 and sample 4, around 0.732. The overall study is showing that as the maturity increases, the pore size distribution is becoming more uniform. The terms D_0–H is utilized to quantify the autocorrelation of the distribution of the porosity over the set of pore sizes related to long-range dependencies (Martínez et al. 2010). The smaller the D_0–H value represents the stronger autocorrelation for the size-dependent pore volume distributions. Sample 5 has the smallest D_0–H value, demonstrating this sample has the strongest autocorrelation in pore size-dependent distribution. The average of the D_0–H value of Sample 1 and Sample 2 is larger than the average value of Sample 3 and Sample 4. Collectively, as the maturity increases, there exists a preference that autocorrelation of the porosity distribution become stronger in our samples.

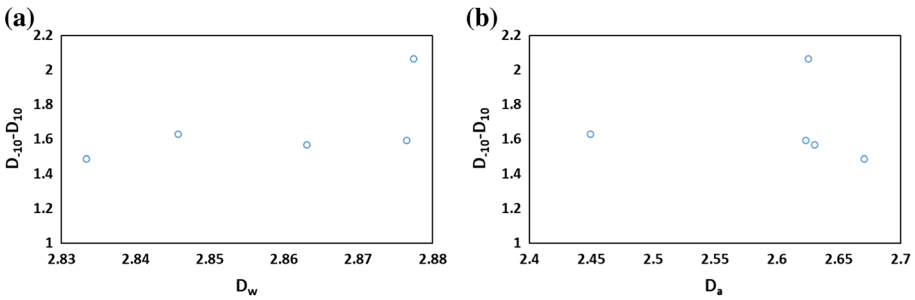

Fig. 12 Correlations between the heterogeneity and the fractal dimension. **a** D_w and **b** D_a

The width of (D_{-10}–D_{10}) can be applied to indicate the heterogeneity degree of pore size distribution. The larger (D_{-10}–D_{10}) value reflects more heterogeneity within the pore size distribution. The average (D_{-10}–D_{10}) value of Sample 1 and Sample 2 is around 1.84685 which is larger than the average value (of 1.57895) of Sample 3 and Sample 4. Sample 5 which is the most mature sample among all has the smallest (D_{-10}–D_{10}) value. As the maturity increases, the pore size distribution will become more homogeneous. This can be interpreted as the thermal advance in the samples will lead to an evolution of larger pores within the organic matter which has been reported in several articles (Chen and Xiao 2014; Liu et al. 2017a, b).

3.6 Correlations Between the Fractal Analysis and Multifractal Analysis

In Sect. 3.3, we analyzed the fractal behavior of pore structures, while Sect. 3.4 was dedicated to multifractal behaviors of the same samples. In the following section, we try to investigate whether there is any correlation between this two-separate analysis. Figure 12 displays the correlations between heterogeneity value (D_{-10}–D_{10}) and D_a and D_w. We were not able to find any robust relationship between D_a and (D_{-10}–D_{10}), D_w and (D_{-10}–D_{10}) which can be inferred that fractal dimension of pore size distribution spectrum as a whole cannot be used to quantify heterogeneity of pore size distributions.

The variation of D_0–D_{10} and D_{-10}–D_0 corresponds to the dominance of large and small pores concentrations, respectively (Yu et al. 2018). Figure 13 is the correlations between D_l and D_0–D_{10}, D_s and D_{-10}–D_0. Strong linear correlations can be found between D_l and D_0–D_{10}, which depicts that variations of multifractal parameters for $q > 0$ are attributed mostly to the larger pores. We failed to establish any relationship between D_s and (D_{-10}–D_0), signifying that smaller pores do not show a major contribution to the variations in multifractal parameters when $q < 0$ (Yu et al. 2018).

3.7 Comparison the Fractal Information from Mercury Intrusion and Nitrogen Gas Adsorption

Nitrogen adsorption is another commonly used method to analyze pore structures of shale samples (Liu et al. 2017a). The comparison between nitrogen adsorption and mercury intrusion data can elevate our understanding of the pore structures of the samples. We also applied thermal dynamic model to calculate the fractal dimension of the entire pore size distribution spectrum from nitrogen gas adsorption data and then calculated the heterogeneity magnitude

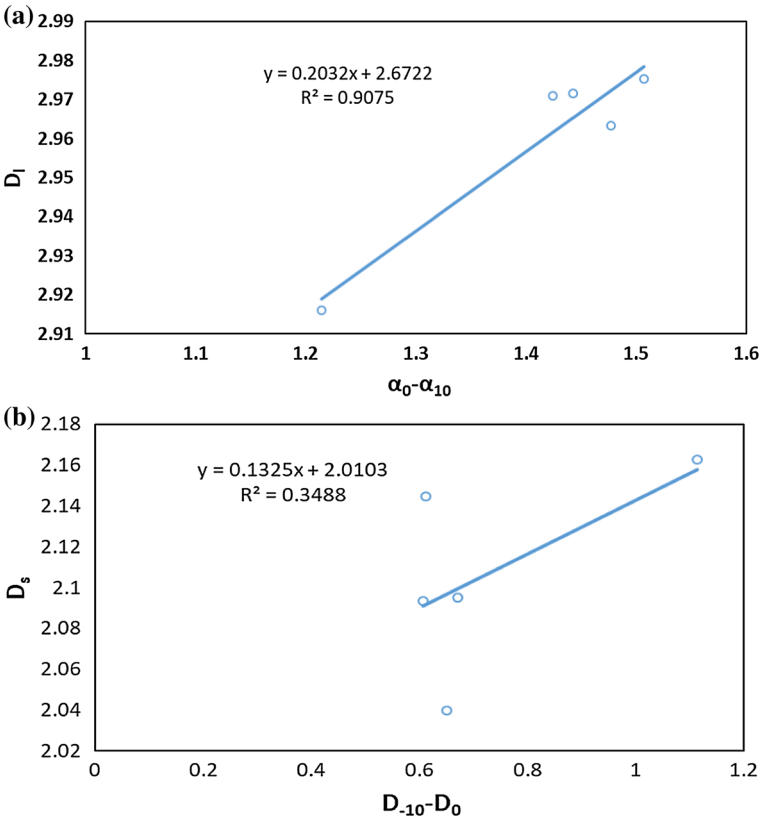

Fig. 13 Correlations between the generalization dimension data and D_l (**a**) and D_s (**b**). **a** (D_0–D_{10}) versus D_l and **b** (D_{-10}–D_0) versus D_s

using the multifractal method. Figure 14 shows the comparison results. Considering the same sample, the D_w from mercury intrusion is larger than D_N from gas adsorption analysis, which is consistent with the results by other scholars (Zhang and Li 1995). Linear correlations can be found between D_N and D_w. The shale sample with larger D_w found to have a larger D_N as well. Though, there was not any correlation between heterogeneity from mercury intrusion and gas adsorption. Sample 5 for instance has the most homogeneous pore structures based on the analysis from mercury intrusion data, while gas adsorption analysis finds this sample with the most heterogeneous pore structures. This is interpreted as nitrogen adsorption, can detect maximum pore size of around 200 nm, while mercury intrusion distinguishes pore with diameter up to a few hundred microns. The heterogeneity that nitrogen adsorption reveals is from pore size in the range of 2–200 nm in diameter, while the heterogeneity that is estimated from mercury intrusion represents pore sizes from 3.6 nm to 200 um in this study. The pore structures of the Bakken shale samples are very complex and heterogeneous that the heterogeneity from the small intervals from the gas adsorption cannot represent the heterogeneity of the larger intervals from high-pressure mercury intrusion.

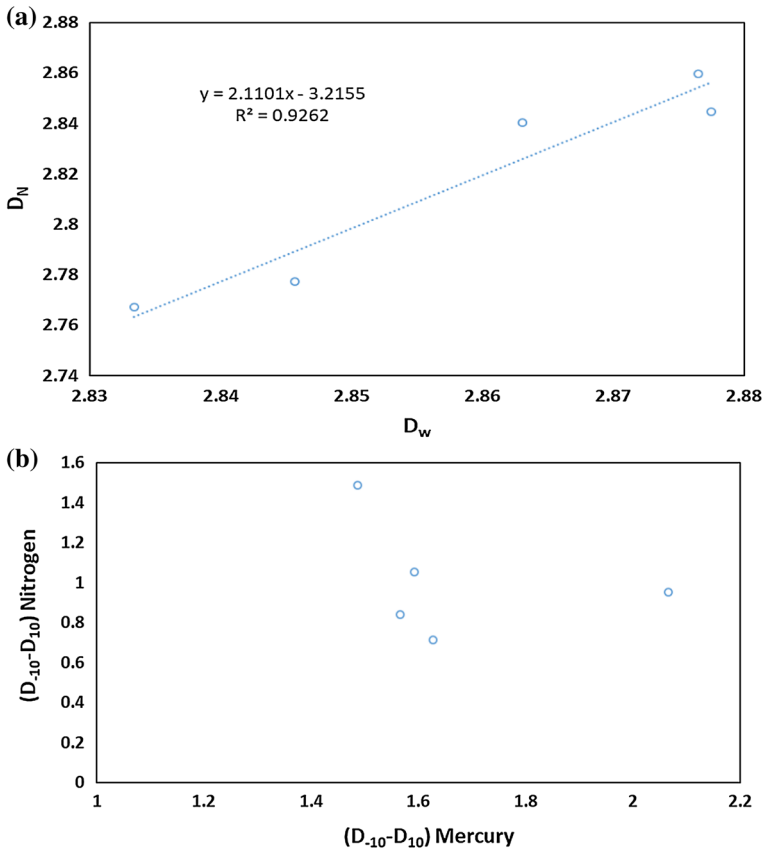

Fig. 14 Fractal analysis comparison between the mercury intrusion and nitrogen gas adsorption. **a** Fractal dimension and **b** heterogeneity comparison

4 Conclusions

Being one of the most widely applied methods for pore structure characterization, high-pressure mercury intrusion was applied in this study to analyze a few samples from the Bakken Shales. Several information regarding the pores of shales such as pore-throat size, pore-throat ratio, fractal and multifractal behaviors is derived and compared. Based on this study, a few conclusions can be made:

1. Hysteresis exists between intrusion and extrusion curves, indicating a complex pore structures in the samples. This infers that large pores are interconnected by smaller pore throats.
2. As the maturity increases, the percentage of large pores to the total pore volume will increase referring to porosity evolution within the organic matter. Pore-throat ratio decreases as the pore-throat size increases. A few inflection points were found in the pore size distributions and the location of the inflection point varies with the samples.
3. The fractal analysis shows that mercury intrusion curve can be subdivided into four segments and the fractal dimension of these four segments follows the order of: $D_l > D_{t1}$

$> D_{f2} > D_s$. The fractal dimension of large pores is largest, while the fractal dimension of the small pores is smallest.

4. The pore structures investigated from mercury intrusion show a multifractal behavior of the samples. The pore size distribution is becoming more uniform as the shale samples are getting more mature. There was not any correlation between fractal dimensions (D_w and D_a) and heterogeneity value (D_{-10}–D_{10}). Larger pores make a significant contribution to multifractal parameters when $q > 0$, while the small pores and transitional pores are the main contributors to the multifractal parameters when $q < 0$.
5. Multifractal analysis of nitrogen gas adsorption and mercury intrusion were compared, and a major discrepancy was pointed out between the results of each, originating from the heterogeneity of the pore structures.

Acknowledgements The authors appreciate the support from China Scholarship Council (No. 201406450029). We would like to also show our appreciation to ND Core Library, Jeff Bader the director and state geologist as well as Kent Holland library technician for providing us with the samples. We thank Dr. Liu from Northeast Petroleum University for running the experiments. We also appreciate the reviewers to give their comments to improve the quality of the paper.

References

Blatt, H., Tracy, R., Owens, B.: Petrology: Igneous, Sedimentary, and Metamorphic. Macmillan, Basingstoke (2006)

Cai, J., Wei, W., Hu, X., Wood, D.A.: Electrical conductivity models in saturated porous media: a review. Earth-Sci. Rev. **171**, 419–433 (2017)

Chaudhuri, B., Sarkar, N.: Texture segmentation using fractal dimension. IEEE Trans. Pattern Anal. **17**(1), 72–77 (1995)

Chen, J., Xiao, X.: Evolution of nanoporosity in organic-rich shales during thermal maturation. Fuel **129**, 173–181 (2014)

Ding, Y., Weller, A., Zhang, Z., Kassab, M.: Fractal dimension of pore space in carbonate samples from Tushka Area (Egypt). Arab. J. Geosci. **10**, 388 (2017)

Ferreiro, J.P., Wilson, M., Vázquez, E.V.: Multifractal description of nitrogen adsorption isotherms. Vadose Zone J. **8**(1), 209–219 (2009)

Giesche, H.: Mercury porosimetry: a general (practical) overview. Part. Part. Syst. Charact. **23**(1), 9–19 (2006)

Hu, Q., Zhang, Y., Meng, X., et al.: Characterization of micro-nano pore networks in shale oil reservoirs of Paleogene Shahejie Formation in Dongying Sag of Bohai Bay Basin, East China. Pet. Explor. Dev. **44**(5), 720–730 (2017)

Kuila, U., Douglas, K., et al.: Nano-scale texture and porosity of organic matter and clay minerals in organic-rich mudrocks. Fuel **135**, 359–373 (2014)

Labani, M.M., Rezaee, R., Saeedi, A., Al Hinai, A.: Evaluation of pore size spectrum of gas shale reservoirs using low pressure nitrogen adsorption, gas expansion and mercury porosimetry: a case study from the Perth and Canning Basins, Western Australia. J. Pet. Sci. Eng. **112**, 7–16 (2013)

Li, J., Yu, T., Liang, X., et al.: Insights on the gas permeability change in porous shale. AGER **1**(2), 69–73 (2017a)

Li, P., Zheng, M., Bi, H., Wu, S., Wang, X.: Pore throat structure and fractal characteristics of tight oil sandstone: a case study in the Ordos Basin, China. J. Pet. Sci. Eng. **149**, 665–674 (2017b)

Li, W., Liu, H., Song, X.: Multifractal analysis of Hg pore size distributions of tectonically deformed coals. Int. J. Coal Geol. **144**, 138–152 (2015)

Liu, K., Ostadhassan, M., Zhou, J., et al.: Nanoscale pore structure characterization of the Bakken shale in the USA. Fuel **209**, 567–578 (2017a)

Liu, K., Ostadhassan, M.: Multi-scale fractal analysis of pores in shale rocks. J. Appl. Geophys. **140**, 1–10 (2017)

Liu, K., Ostadhassan, M., Gentzis, T., et al.: Characterization of geochemical properties and microstructures of the Bakken Shale in North Dakota. Int. J. Coal Geol. **190**, 84–98 (2018a)

Liu, K., Ostadhassan, M., Zou, J., et al.: Multifractal analysis of gas adsorption isotherms for pore structure characterization of the Bakken Shale. Fuel **219**, 296–311 (2018b)

Liu, K., Ostadhassan, M., Zhou, J., et al.: Nanopore structures of isolated kerogen and bulk shale in Bakken Formation. Fuel **226**, 441–453 (2018c)
Liu, Y., Xiong, Y., Li, Y., Peng, P.A.: Effects of oil expulsion and pressure on nanopore development in highly mature shale: evidence from a pyrolysis study of the Eocene Maoming oil shale, south China. Mar. Pet. Geol. **86**, 526–536 (2017b)
Liu, Z., Pan, Z., Zhang, Z., Liu, P., Shang, L., Li, B.: Effect of porous media and sodium dodecyl sulphate complex system on methane hydrate formation. Energy Fuels **32**(5), 5736–5749 (2018d)
Lopes, R., Betrouni, N.: Fractal and multifractal analysis: a review. Med. Image Anal. **13**(4), 634–649 (2009)
Mandelbrot, B.B.: The Fractal Geometry of Nature, vol. 173. WH Freeman, New York (1983)
Mandelbrot, B.B., Passoja, D.E., Paullay, A.J.: Fractal character of fracture surfaces of metals. Nature **308**, 721–722 (1984)
Martínez, F.S.J., Martín, M.A., Caniego, F.J., Tuller, M., Guber, A., Pachepsky, Y., García-Gutiérrez, C.: Multifractal analysis of discretized X-ray CT images for the characterization of soil macropore structures. Geoderma **156**(1–2), 32–42 (2010)
Paz Ferreiro, J., Miranda, J.G.V., Vidal Vázquez, E.: Multifractal analysis of soil porosity based on mercury injection and nitrogen adsorption. Vadose Zone J. **9**(2), 325–335 (2010)
Peng, C., Zou, C., Yang, Y., Zhang, G., Wang, W.: Fractal analysis of high rank coal from southeast Qinshui basin by using gas adsorption and mercury porosimetry. J. Pet. Sci. Eng. **156**, 235–249 (2017)
Posadas, A.N., Giménez, D., Bittelli, M., Vaz, C.M., Flury, M.: Multifractal characterization of soil particle-size distributions. Soil Sci. Soc. Am. J. **65**(5), 1361–1367 (2001)
Russel, D.A., Hanson, J., Ott, E.: Dimension of strange attractors. Phys. Rev. Lett. **45**(14), 1175–1178 (1980)
Schlömer, S., Krooss, B.M.: Experimental characterisation of the hydrocarbon sealing efficiency of cap rocks. Mar. Pet. Geol. **14**(5), 565–580 (1997)
Schmitt, M., Fernandes, C.P., da Cunha Neto, J.A., Wolf, F.G., dos Santos, V.S.: Characterization of pore systems in seal rocks using nitrogen gas adsorption combined with mercury injection capillary pressure techniques. Mar. Pet. Geol. **39**(1), 138–149 (2013)
Thompson, A.H., Katz, A.J., Krohn, C.E.: The micro-geometry and transport properties of sandstones. Adv. Phys. **36**(5), 625–694 (1987)
Washburn, E.W.: The dynamics of capillary flow. Phys. Rev. **17**(3), 273 (1921)
Webb, P.A.: An Introduction to the Physical Characterization of Materials by Mercury Intrusion Porosimetry with Emphasis on Reduction and Presentation of Experimental Data. Micromeritics Instrument Corp, Norcross (2001)
Xia, Y., Cai, J., Wei, W., Hu, X., Wang, X., Ge, X.: A new method for calculating fractal dimensions of porous media based on pore size distribution. Fractals **26**(1), 1850006 (2018)
Yang, Y., Zhang, W., Gao, Y., et al.: Influence of stress sensitivity on microscopic pore structure and fluid flow in porous media. J. Nat. Gas Sci. Eng. **36**(Part A), 20–31 (2016)
Yu, S., Bo, J., Pei, S., et al.: Matrix compression and multifractal characterization for tectonically deformed coals by Hg porosimetry. Fuel **211**, 661–675 (2018)
Zhang, B., Li, S.: Determination of the surface fractal dimension for porous media by mercury porosimetry. Ind. Eng. Chem. Res. **34**(4), 1383–1386 (1995)
Zhang, Z., Weller, A.: Fractal dimension of pore-space geometry of an Eocene sandstone formation. Geophysics **79**(6), D377–D387 (2014)
Zhang, P., Lu, S., Li, J., et al.: Permeability evaluation on oil-window shale based on hydraulic flow unit: a new approach. AGER **2**(1), 1–13 (2017)
Zhou, S., Liu, D., Cai, Y., Yao, Y., Che, Y., Liu, Z.: Multi-scale fractal characterizations of lignite, subbituminous and high-volatile bituminous coals pores by mercury intrusion porosimetry. J. Nat. Gas Sci. Eng. **44**, 338–350 (2017)